Article:

Ge, R., Li, Q., Li, C. et al. (1 more author) (2022) Evaluation of different melting performance enhancement structures in a shell-and-tube latent heat thermal energy storage system. Renewable Energy, 187. pp. 829-843. ISSN 0960-1481

https://doi.org/10.1016/j.renene.2022.01.097

Evaluation of different melting performance enhancement structures in a shell-and-tube latent heat thermal energy storage system

Ruihuan Ge [a], Qi Li [b], Chuan Li [b*], Qing Liu [c]

[a] Department of Chemical and Biological Engineering, University of Sheffield, Sheffield S10 2TN, UK

[b] MOE Key Laboratory of Enhanced Heat Transfer and Energy Conservation, Beijing Key Laboratory of Heat Transfer and Energy Conversion, Beijing University of Technology, Beijing, 100124, China

[c] School of Energy and Environmental Engineering, University of Science and Technology Beijing, Beijing 100083, China

[*]Corresponding Email: r.ge@sheffield.ac.uk; lichuan0315@hotmail.com

Abstract

Latent heat thermal energy storage employing phase change materials are widely used in energy storage systems. To further improve the low thermal conductivity of phase change materials in these systems, it is essential to investigate different thermal enhancement techniques. In this work, two principal thermal enhancement techniques, e.g. finned tubes and conductive metal foams are numerically investigated for melting processes in a shell-and-tube latent heat thermal energy storage system. For fins the topology optimised fins are used, and the simulation predictions are validated by experimental results using additive manufactured topology optimised fins. For metal foams two configurations with different filling ratios, i.e. whole-foam structure and half-foam structure are considered. Compared to the configuration without enhancement, the thermal energy storage rates are 3.3-5.8 times higher. In addition, the results show that the topology optimised fins can achieve the best performance, but can only be an economical solution when the unit price ratio between the enhancement technique and the phase change materials is less than 6. For the first time the thermal enhancement performance and economic efficiency of these two principal techniques are quantitatively analysed. The results would be useful for appropriate energy storage design solutions in practice.

Key words: Phase change material (PCM), Latent heat thermal energy storage (LHTES), Melting, Shell-and-tube device, Additive manufacturing

1. Introduction

Nowadays, with the increased demand for renewable energy, energy storage systems are desired to deal with the mismatched supply and demand of energy, and to further enhance the system performance. The latent heat thermal energy storage (LHTES) techniques are attractive due to advantages of reasonable investment and high energy density. In a LHTES system, phase change materials (PCMs) are used to charge/discharge thermal energy during melting/solidification [1]. One of the most common LHTES techniques are shell-and-tube LHTES systems, with the PCMs filling in the shell while the low/high temperature heat transfer fluid (HTF) flowing through the internal tubes. For this system, one main barrier that needs to be tackled is the heat transfer enhancement within the low thermal conductivity PCMs.

Substantial investigations have been carried out to enhance the heat transfer at the PCM side of the shell-and-tube LHTES device. Relevant techniques that have been applied include finned tubes, PCM with metal foam and nanoparticle-enhanced PCMs [1]. Fins or extended surfaces are the most common way for performance enhancement. Various fin configurations have been proposed and investigated by researchers, such as longitudinal fin [2], annular fin [3], helical fin [4] and bifurcated fin [5]. The results have demonstrated that the discharging/charging process can be significantly shortened by using fin surfaces. The effects of fin dimensions (e.g. length, orientation and thickness) [6-8], pipe configurations [9] on the device performance have been thoroughly investigated. Especially, previous research has showed that fin configurations affect the melting performance. The optimised fin configuration angles during melting were investigated by Kazemi et al. [10] and Mahood et al. [11]. Due to the natural convection effect, the fins concentrate at the lower part of the shell are more effective to reduce the melting time when the device is placed horizontally. Nevertheless, the proposed fin configurations are limited by design freedoms and the optimised selection criterion is scarce. Recently, Pizzolato et al. [12] applied topology optimisation algorithm to design the fin layouts of shell-and-tube LHTES systems. They firstly obtained the optimised fin layouts of the discharge process, in both two-dimenaional (2D) and three-dimensional (3D) domain. The topology optimised 3D design shows a mixture feature of longitudinal fins, angular fins, and pin fins [12]. The natural convection effect was considered for the fin designs through topology optimisation. The optimised fin designs can be 37 % and 17 % faster charge and discharge compared to the conventional longitudinal fins [13]. The topology optimised results of multi-tube configurations were further obtained, and additive manufacturing was used to demonstrate the manufacturability of topology optimised fins [14].

Impregnation of porous foams is another commonly used technique to improve the heat transfer of LHTES device as the porous foams made of copper or aluminium have high heat transfer surface areas and high thermal conductivities. The effects of various influential factors of the porous foams such as inlet fluid conditions [15], configurations [16], foam porosity [17, 18] and hypergravity [19] have been investigated numerically and experimentally. The geometric factors of porous foams have a significant impact on the performance of LHTES device. During melting, the insertion of metal foams can restrict the flow motion and have passive effects on the natural convection. Recently effects of porosity-variability, partial foam have been further investigated to understand how this configuration affects the PCM melting. Yang et al. [20] proposed a metal foam structure with linearly changed porosity. The results showed that the linear increased porosity from bottom could enhance narural convection and and shorten the melting time. Recently, the gradient foam design design has been applied to the shell-and-tube LHTES device. Pu et al. [21] numerically investigated the effect of gradient copper foam on the melting performance. A radial gradient porosity (0.99-0.97-0.87) was recommended that can further reduce the melting time by 23.7%. A 2D gradient porosity along radial and circumferential direction is proposed by Yang et al. [22], the melting time can be reduced by 32.11% compared with the uniform structure. Xu et al. [23] investigated the effect of foam arrangements on the melting process, and found that the optimal filling ratio of the foams is 0.7 for a horizontal shell-and-tube LHTES device. Smiliar partial foam approach have been applied to the rectangular cavity [24]. In general, the partial foam concentrated in the lower part of the device would be useful to enhance the heat transfer and reduce the melting time [25].

Recently the combination of different thermal enhancement techniques in a LHTES device is also attracting attention. Yang et al. [26] numerically investigated the fin-metal-foam TES device, a further heat enhancement can be achieved by combining fins and metal foams. An experimental study was performed by Guo et al. [27], a reduction of 83.35% melting time can be achieved compared with the conventional device without thermal enhancement. An alternative methodology to enhance the thermal response is the application of nanoparticles [28]. The dispersion of high thermal conductivity nanoparticles can shorten the melting and solidification time. However, the addition of nanoparticles can increase the fluid viscosity and cause natural convection suppression [29]. Some researchers reported the use of a combination fin and nanoparticles, they found that the addition of nanoparticles cannot improve the melting process in the heat conduction dominated region [30], and a better enhancement can be achieved by purely adding fins when using the same volume materials [31].

As the natural convection effects during melting can be inhibited by extended fin surfaces and foams, understanding how these thermal ehhancement techniques affect the melting performance is important. Meanwhile, there is a lack of research in literature to quantitatively compare and evaluate the performance of different heat transfer enhancement methods for the shell-and-tube LHTES device. Even if some optimised configurations have been proposed, a compresenhensive comparison and evaluation of these techniques is still necessary. In this work, 2D computational fluid dynamics (CFD) models were developed to evaluate the performance of the topology optimised fins and porous foams for the melting process in the LHTES system. An additive manufactured device was used to validate the model predictions for the topology optimised fins. Different configurations, i.e. single-tube and four-tube were considered. Qualitative and quantitative comparisons were made in the end between different cases under same operation conditions and PCM volumes.

2. Methodology

2.1 System description

The schematic diagram of the LHTES devices and detailed dimensions used in this work are illustrated in Figure 1. The effect of tube configurations, i.e. single-tube and four-tube was considered for all cases.

Figure 1 (a) illustrates topology optimised fins with special configurations for melting process. Both natural convection and conduction effects were considered during topology optimisation [13, 32]. This configuration could help to enhance heat transfer via both convection and conduction. The high conductivity fins mainly concentrate in the conduction dominated bottom region which is particularly obvious for the single-tube configuration. For making a better comparison with the topology optimised fins, two different conductive foam configurations are considered. In Figure 1 (b) the metal foam is only filled the lower half region, while in Figure 1 (c) the metal foam is fully filled the region. In the following, they are also named as half-foam structure and whole-foam structure, respectively. For all cases, the volume fraction of the high conductivity aluminium alloy was set to 10% of the whole domain, and correspondingly the PCM occupies 90% of the investigated domain.

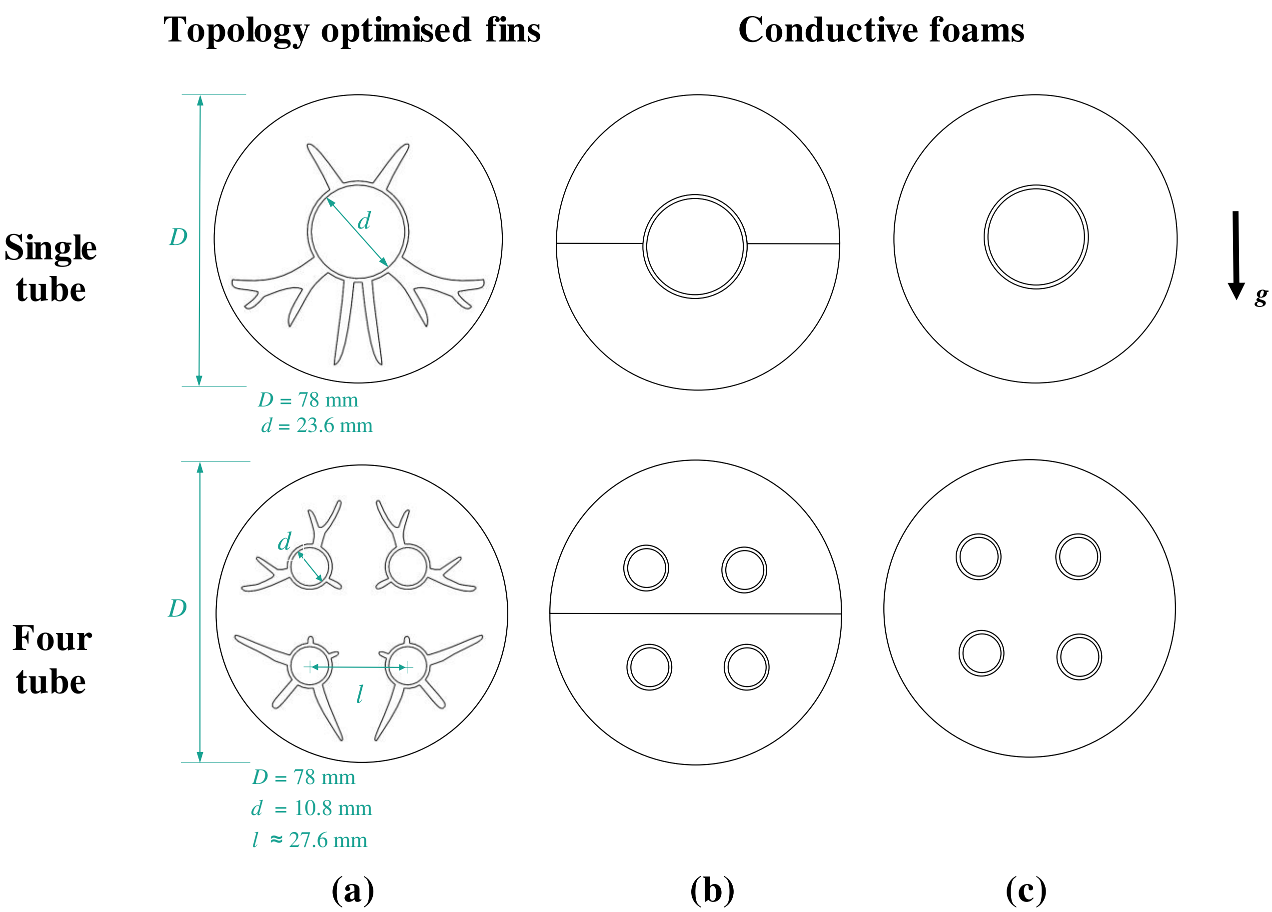

Figure 1. Schematic diagram of the LHTES devices . (a) Topology structure. (b) Half-foam structure. (c) Whole-foam structure. The arrow shows the gravity direction.

2.2 Mathematical model

The enthalpy-porosity approach was used for simulation of PCM melting [33]. The temperature and the velocity of the PCM during melting can be calculated using the Navier-Strokes equations. A commercial paraffin RT25 HC (Rubitherm GmbH) was used as PCM materials, and the physical properties are listed in Table 1 [34]. In this work, the temperature-dependent function of viscosity is not considered. This is in accordance with the previous topology optimisation simulations and some relevant research works using RT 25HC PCM [14, 35]. The effect of temperature on the viscosity can be further investigated in future. The physical properties of aluminium alloy used for topology optimised fins and conductive foams are listed in Table 2 [36].

As the main focus of this work is on the evolutions of the liquid fraction and temperature along the radial direction, 2D domain with isothermal heating boundary of inner tube is investigated. The fluid temperature variation in the inner tubes and relevant 3D effects are not investigated in this work. The governing equations have different forms according to different systems.

2.2.1 Topology optimised fins

By using topology optimisation algorithm, the high conductive fin configurations can be optimised in the whole domain. Detailed topology optimisation procedure have been reported in previous work [13, 32]. In the following, the topology optimised fins for melting are used for performance evaluation.

The continuity equation is:

$$\frac{\partial u}{\partial x}+\frac{\partial v}{\partial y}=0 \tag{1}$$

where u and v are the fluid velocities in x and y directions.

The momentum equations at two different directions are:

$$\rho_{\mathrm{P}}\left(\frac{\partial u}{\partial t}+u\frac{\partial u}{\partial x}+v\frac{\partial u}{\partial y}\right)=\mu_{\mathrm{P}}\left(\frac{\partial^2 u}{\partial x^2}+\frac{\partial^2 u}{\partial y^2}\right)-\frac{\partial p}{\partial x}+\frac{(1-\beta)^2}{(\beta^3+\omega)}A_{\mathrm{m}}u \tag{2}$$

$$\rho_{\mathrm{P}}\left(\frac{\partial v}{\partial t}+u\frac{\partial v}{\partial x}+v\frac{\partial v}{\partial y}\right)=\mu_{\mathrm{P}}\left(\frac{\partial^2 v}{\partial x^2}+\frac{\partial^2 v}{\partial y^2}\right)-\frac{\partial p}{\partial y}+\frac{(1-\beta)^2}{(\beta^3+\omega)}A_{\mathrm{m}}v-\rho_{\mathrm{P}}g\gamma_{\mathrm{P}}(T-T_{\mathrm{ref}}) \tag{3}$$

where ρ_{P} is the PCM density, t is time, μ_{P} is dynamic viscosity, p is effective pressure, T is temperature, γ_{P} is thermal expansion coefficient. ω is a small constant number (0.0001) to avoid division by zero which has been used by previously PCM melting simulations [13, 15]. A_{m} (10^8 kg·m^{-3}·s^{-1}) is the mushy constant that describes how sharply the velocity is reduced to zero when the PCM solidifies. β is the liquid fraction of PCM that can be given by:

$$\beta=\begin{cases} 0 & if\ T<T_{\mathrm{s}} \\ \dfrac{T-T_{\mathrm{s}}}{T_{\mathrm{l}}-T_{\mathrm{s}}} & if\ T_{\mathrm{s}}<T<T_{\mathrm{l}} \\ 1 & if\ T>T_{\mathrm{l}} \end{cases} \tag{4}$$

In this work, T_{l} is 295 K, and T_{s} is 299 K (Table 1).

The governing energy equation of PCM phase is:

$$\rho_{\mathrm{P}} C_{\mathrm{p,P}} \left(\frac{\partial T}{\partial t} + u \frac{\partial T}{\partial x} + v \frac{\partial T}{\partial y} \right) = \frac{\partial}{\partial x} \left(k_{\mathrm{P}} \frac{\partial T}{\partial x} \right) + \frac{\partial}{\partial y} \left(k_{\mathrm{P}} \frac{\partial T}{\partial y} \right) - L_{\mathrm{P}} \frac{\partial \beta}{\partial t} \tag{5}$$

where $C_{\mathrm{p,P}}$ is the specific heat of PCM, k_{P} is the thermal conductivity of PCM, L_{P} is the latent heat.

The governing energy equation of the topology optimised fins made of aluminium alloy can be written as:

$$\rho_{\mathrm{M}} C_{\mathrm{p,M}} \frac{\partial T}{\partial t} = \frac{\partial}{\partial x} \left(k_{\mathrm{M}} \frac{\partial T}{\partial x} \right) + \frac{\partial}{\partial y} \left(k_{\mathrm{M}} \frac{\partial T}{\partial y} \right) \tag{6}$$

where $C_{\mathrm{p,M}}$ is the specific heat of aluminium alloy, k_{M} is the thermal conductivity of aluminium alloy.

Table 1 Thermophysical properties of RT25 HC PCM [34].

Description	Parameter	
Density of solid (kg·m^{-3})	ρ_{P}	880
Melting range (K)	ΔT	295-299
Latent heat (kJ·kg^{-1})	L_{P}	232
Thermal conductivities solid/liquid (W·m^{-1}·K^{-1})	k_{P}	0.2
Specific heat (kJ·kg^{-1}·K^{-1})	$C_{\mathrm{p,P}}$	2
Viscosiy (kg·m^{-1}·s^{-1})	μ_{P}	0.001798
Thermal expansion coefficient (K^{-1})	γ_{P}	0.001

Table 2. Thermophysical properties of aluminium alloy [36].

Description	Parameter	
Density of solid (kg·m^{-3})	ρ_{M}	2700
Thermal conductivity (W·m^{-1}·K^{-1})	k_{M}	160
Specific heat (kJ·kg^{-1}·K^{-1})	$C_{\mathrm{p,M}}$	0.9

2.2.2 Conductive foam

The conductive foam embedded in PCM phase provides a promising way to enhance heat transfer during melting process. A mathematical model has been developed to describe the whole process in porous media [15].

The momentum equations are:

$$\rho_{\mathrm{P}}\left(\frac{\partial u}{\partial t}+u\frac{\partial u}{\partial x}+v\frac{\partial u}{\partial y}\right)=\mu_{\mathrm{P}}\left(\frac{\partial^2 u}{\partial x^2}+\frac{\partial^2 u}{\partial y^2}\right)-\frac{\partial p}{\partial x}+\frac{(1-\beta)^2}{(\beta^3+\omega)}A_{\mathrm{m}}u+\frac{\mu_{\mathrm{P}}}{a}u+\frac{1}{2}C_{\mathrm{i}}\rho u|u| \tag{7}$$

$$\rho_{\mathrm{P}}\left(\frac{\partial v}{\partial t}+u\frac{\partial v}{\partial x}+v\frac{\partial v}{\partial y}\right)=\mu_{\mathrm{P}}\left(\frac{\partial^2 v}{\partial x^2}+\frac{\partial^2 v}{\partial y^2}\right)-\frac{\partial p}{\partial y}+\frac{(1-\beta)^2}{(\beta^3+\omega)}A_{\mathrm{m}}v-\rho_{\mathrm{P}}g\gamma_{\mathrm{P}}(T-T_{\mathrm{ref}})+\frac{\mu_{\mathrm{P}}}{a}v+\frac{1}{2}C_{\mathrm{i}}\rho_{\mathrm{P}}v|v| \tag{8}$$

The viscous resistance and the inertia resistance at two different directions are considered in the momentum equations. The definition of permeability a and the inertia coefficient C_{i} are given in the following sections. Due to the low velocities during melting process, the inertia resistance has insignificant effect on the results.

A non-equribrium thermal model is used to describe the porous media:

$$\varepsilon\rho_{\mathrm{P}}C_{\mathrm{p,P}}\frac{\partial T}{\partial t}+\rho_{\mathrm{P}}C_{\mathrm{p,P}}\left(u\frac{\partial T}{\partial x}+v\frac{\partial T}{\partial y}\right)=(k_{\mathrm{fe}}+k_{\mathrm{td}})\left(\frac{\partial^2 T}{\partial x^2}+\frac{\partial^2 T}{\partial y^2}\right)+h_{\mathrm{sf}}A_{\mathrm{sf}}(T_{\mathrm{f}}-T_{\mathrm{s}})-\varepsilon\rho_{\mathrm{P}}L_{\mathrm{P}}\frac{\partial\beta}{\partial t} \tag{9}$$

$$(1-\varepsilon)\rho_{\mathrm{M}}C_{\mathrm{p,M}}\frac{\partial T}{\partial t}=k_{\mathrm{se}}\left(\frac{\partial^2 T}{\partial x^2}+\frac{\partial^2 T}{\partial y^2}\right)+h_{\mathrm{sf}}A_{\mathrm{sf}}(T_{\mathrm{s}}-T_{\mathrm{f}}) \tag{10}$$

where ε is the porosity of the conductive foam. k_{fe} and k_{se} are the effective thermal conductivities of the PCM and foam. k_{td} is used to describe the effect of thermal dispersion. A_{sf} is the surface area density, and h_{sf} is heat transfer coefficient between PCM and the porous foam.

(1) Permeability and inertial coefficient

The permeability a and the inertia coefficient C_{i} can be calculated by the following equations [37]:

$$a=0.00073(1-\varepsilon)^{-0.224}d_{\mathrm{f}}^{-1.11}d_{\mathrm{p}}^{0.89} \tag{11}$$

$$C_{\mathrm{i}}=0.00212(1-\varepsilon)^{-0.132}\left(\frac{d_{\mathrm{f}}}{d_{\mathrm{p}}}\right)^{-1.63} \tag{12}$$

The cell ligament d_{f} and the pore size d_{p} can be defined as [37]:

$$\frac{d_{\mathrm{f}}}{d_{\mathrm{p}}}=1.18\sqrt{\frac{1-\varepsilon}{3\pi}}\left(\frac{1}{1-e^{-(1-\varepsilon)/0.04}}\right) \tag{13}$$

(2) Effective thermal conductivity and the effects of thermal dispersion

The effective thermal conductivities of the PCM k_{fe} and the metal foam k_{se} are calculated from a tetrakaidecahedron model [38]:

$$k_{\mathrm{fe}} = \left.\frac{\sqrt{2}}{2(M_{\mathrm{A}} + M_{\mathrm{B}} + M_{\mathrm{C}} + M_{\mathrm{D}})}\right|_{k_{\mathrm{M}}=0} \tag{14}$$

$$k_{\mathrm{se}} = \left.\frac{\sqrt{2}}{2(M_{\mathrm{A}} + M_{\mathrm{B}} + M_{\mathrm{C}} + M_{\mathrm{D}})}\right|_{k_{\mathrm{P}}=0} \tag{15}$$

$$M_{\mathrm{A}} = \frac{4\sigma}{\left(2e^2 + \pi\sigma(1-e)\right)k_{\mathrm{M}} + \left(4 - 2e^2 - \pi\sigma(1-e)\right)k_{\mathrm{P}}} \tag{16}$$

$$M_{\mathrm{B}} = \frac{(e-2\sigma)^2}{(e-2\sigma)e^2 k_{\mathrm{M}} + (2e - 4\sigma - (e-2\sigma)e^2)k_{\mathrm{P}}} \tag{17}$$

$$M_{\mathrm{C}} = \frac{\left(\sqrt{2} - 2e\right)^2}{2\pi\sigma^2\left(1 - 2e\sqrt{2}\right)k_{\mathrm{M}} + 2\left(\sqrt{2} - 2e - \pi\sigma^2\left(1 - 2e\sqrt{2}\right)\right)k_{\mathrm{P}}} \tag{18}$$

$$M_{\mathrm{D}} = \frac{2e}{e^2 k_{\mathrm{M}} + (4 - e^2)k_{\mathrm{P}}} \tag{19}$$

$$\sigma = \sqrt{\frac{\sqrt{2}\left(2 - \frac{5}{8e^3\sqrt{2}} - 2e\right)}{\pi\left(3 - 4e\sqrt{2} - e\right)}} \tag{20}$$

$$e = 0.339 \tag{21}$$

The thermal dispersion conductivity is derived from a dimensionless thermal dispersion model proposed by Georgiadis and Catton [39]:

$$k_{\mathrm{td}} = \frac{0.36}{1-\varepsilon}\rho_{\mathrm{P}} C_{\mathrm{p,P}} d_{\mathrm{f}} \sqrt{u^2 + v^2} \tag{22}$$

(3) Interfacial heat-transfer coefficient

The heat transfer coefficient was estimated using Churchill and Chu [40] correlation:

$$h_{\mathrm{sf}} = \frac{k_{\mathrm{P}}}{d_{\mathrm{f}}}\left(0.36 + \frac{0.518 Ra_{\mathrm{d}}^{1/4}}{\left[1 + \left(\frac{0.599}{Pr}\right)^{9/16}\right]}\right) \tag{23}$$

$$Ra_{\mathrm{d}} = \frac{g\gamma |T_{\mathrm{f}} - T_{\mathrm{s}}| d_{\mathrm{f}}^3}{\alpha_{\mathrm{f}} \nu_{\mathrm{f}}} \tag{24}$$

where T_{f} and T_{s} are the temperature of fluid and solid phases, α_{f} is the thermal diffusivity, and ν_{f} is the kinematic viscosity.

The specific surface area A_{sf} of the metal foams can be calculated by [37]:

$$A_{\mathrm{sf}} = \frac{3\pi d_{\mathrm{f}}\left(1 - e^{-(1-\varepsilon)/0.04}\right)}{\left(0.59 d_{\mathrm{p}}\right)^2} \tag{25}$$

2.2.3 Performance evaluation

Two parameters, average thermal energy storage rate, p_{ave}, and average thermal energy storage density, q_{ave}, are introduced to evaluate the performance of different structured configurations [23] :

$$p_{\mathrm{ave}} = \frac{Q}{t_{\mathrm{m}}} = \frac{m_{\mathrm{M}} \int c_{\mathrm{p,M}} dT + m_{\mathrm{P}} (\int c_{\mathrm{ps,P}} dT + L + \int c_{\mathrm{pl,P}} dT)}{t_m} \tag{26}$$

$$q_{\mathrm{ave}} = \frac{Q}{m} = \frac{m_{\mathrm{M}} \int c_{\mathrm{p,M}} dT + m_{\mathrm{P}} (\int c_{\mathrm{ps,P}} dT + L + \int c_{\mathrm{pl,P}} dT)}{m_{\mathrm{P}} + m_{\mathrm{M}}} \tag{27}$$

where m_{M} and m_{P} are respectively the mass of enhanced structure and PCM. The p_{ave} refers to the device thermal energy storage capacity per unit charging time while q_{ave} indicates the device capacity per unit material amount. For a PCM based device particularly for these containing low temperature PCM, i.e., the paraffin in this work, the great majority of heat will be stored through the latent heat form, and the sensible heat of the enhanced structure and PCM can be ignored [23]. Therefore, the Equations (26) and (27) can be simplified as follows:

$$p_{\mathrm{ave}} = \frac{m_{\mathrm{P}} L}{t_{\mathrm{m}}} \tag{28}$$

$$q_{\mathrm{ave}} = \frac{m_{\mathrm{P}} L}{m_{\mathrm{P}} + m_M} \tag{29}$$

Given dimensionless transformation, the above two equations can be further changed to:

$$p'_{\mathrm{ave}} = \frac{p_{\mathrm{ave}}}{p_{\mathrm{ave,0}}} = \frac{m_{\mathrm{P}} L / t_{\mathrm{m}}}{m_{\mathrm{P,0}} L / t_{\mathrm{m,0}}} = \frac{m_{\mathrm{P}} t_{\mathrm{m,0}}}{m_{\mathrm{P,0}} t_{\mathrm{m}}} \tag{30}$$

$$q'_{\mathrm{ave}} = \frac{q_{\mathrm{ave}}}{q_{\mathrm{ave,0}}} = \frac{m_{\mathrm{P}} L / (m_{\mathrm{P}} + m_{\mathrm{M}})}{m_{\mathrm{P,0}} L / m_{\mathrm{P,0}}} = \frac{m_{\mathrm{p}}}{m_{\mathrm{P}} + m_{\mathrm{M}}} \tag{31}$$

where the $p_{\mathrm{ave,0}}$ and $q_{\mathrm{ave,0}}$ respectively relate to the average TES rate and density of the configuration without enhancement structure.

A parameter of TES rate per material cost p_{c} is also introduced for determining the device input-output performance and its formula can be expressed as follows:

$$p_{\mathrm{c}} = \frac{Q}{t_{\mathrm{m}} S} = \frac{m_{\mathrm{M}} \int c_{\mathrm{p,M}} dT + m_{\mathrm{P}} (\int c_{\mathrm{ps,P}} dT + L + \int c_{\mathrm{pl,p}} dT)}{t_{\mathrm{m}} (a_{\mathrm{M}} m_{\mathrm{M}} + a_{\mathrm{P}} m_{\mathrm{p}})} \approx \frac{m_{\mathrm{P}} L}{t_{\mathrm{m}} (a_{\mathrm{M}} m_{\mathrm{M}} + a_{\mathrm{P}} m_{\mathrm{P}})} \tag{32}$$

$$p'_{\mathrm{c}} = \frac{p_{\mathrm{c}}}{p_{\mathrm{c,0}}} = \frac{m_{\mathrm{P}} L}{t_{\mathrm{m}} (a_{\mathrm{M}} m_{\mathrm{M}} + a_{\mathrm{P}} m_{\mathrm{P}})} \Big/ \frac{m_{\mathrm{P,0}} L}{t_{\mathrm{m,0}} m_{\mathrm{P,0}} a_{\mathrm{P}}} = \frac{m_{\mathrm{P}}}{t_{\mathrm{m}} / t_{\mathrm{m,0}} (R m_{\mathrm{M}} + m_{\mathrm{P}})} \tag{33}$$

where S represents the total material cost of the PCM and enhancement structures. a indicates the unit price. p'_{c} is the dimensionless form of p_{c} which stands for the ratio between p_{c} and $p_{\mathrm{c,0}}$. R means unit price ratio of the enhancement structures to the PCM:

$$R = a_{\mathrm{M}} / a_{\mathrm{P}} \tag{34}$$

where a_{M} is the unit price the enhancement technique, and a_{P} is the unit price of PCM.

2.3 Numerical schemes and validation

CFD simulations of different systems were carried out using ANSYS FLUENT 2019. A software of GAMBIT 2.2 was used for mesh building. The finite volume method (FVM) was adopted to discretise the governing equation with the PRESTO scheme and the SIMPLEC algorithm being respectively employed for the pressure correction equation and pressure-velocity coupling. A scheme of second-order upwind was used for discretising the momentum and energy terms.

A schematic view of the model design for CFD simulations on topology structure is illustrated in Figure 2. In simulations, due to the symmetry of the systems, only the left half of the domain needs to be considered (Figure 2). For all systems, the initial temperature of the solid PCM is T_{ini}=294.5 K, and the temperature of the inlet wall is T_{in}=308 K. Mesh independence study was performed considering different cell numbers. The liquid fraction (β) values considering different cell numbers are shown in Table 3. In this work, 1.2x10^5 cells were adopted to ensure the results reliability. Time step independence analysis is shown in Table 4. From Table 4, a time step of 0.05 s is sufficient to ensure time step independence.

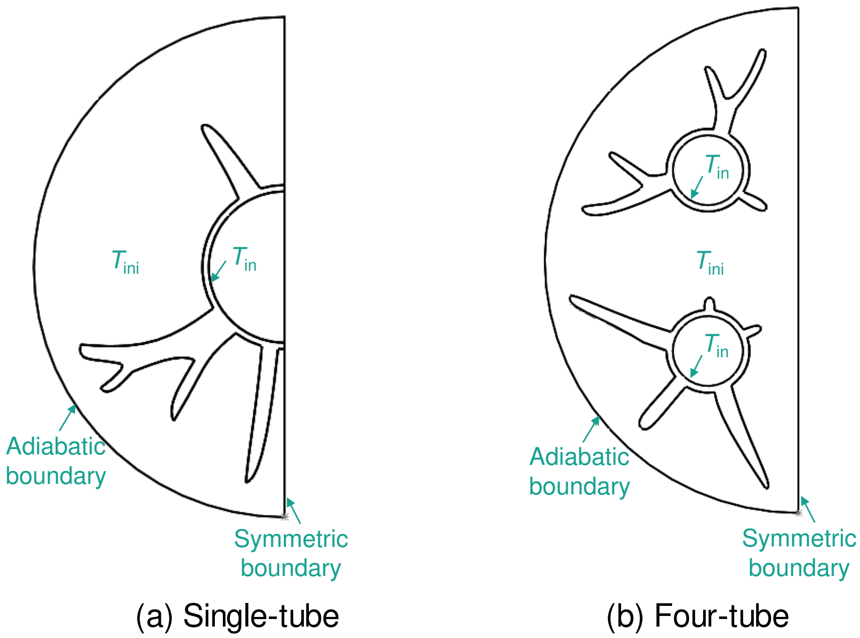

Figure 2. Schematic view of the model design for CFD simulations.

Table 3. The liquid fraction (β) values considering different cell numbers.

	800 s	1600 s	3200 s	4000 s
6x10^4 cells	0.396	0.614	0.939	1.0
1.2x10^5 cells	0.398	0.623	0.947	1.0
2x10^5 cells	0.394	0.618	0.946	1.0

Table 4. Time step independence analysis.

	Time step (s)	Melting time (s)	Deviation from reference case (%)
Test 1	0.1	4222	13
Test 2	0.05	3753	0.48
Reference case	0.025	3735	-

The validation for the partial-porous model by comparing the present model predictions with modelling results from [25] under the same operation and geometrical conditions is shown in Figure 4. A horizontal shell-and-tube configuration with external diameter of 62.5 mm and internal diameter of 20 mm was modelled with a binary salt of Li_2CO_3-K_2CO_3 with mole ratio of 62:38 used as PCM. A parameter of the angle between neighbouring metal foam (*b*) was employed to investigate the metal foam volume effects on the melting process. One can see from Figure 4 that, for the selected different *b* (0°, 30° and 60°), reasonably well agreements between the current model and numerical results have been achieved with an average deviation less than 5% observed, demonstrating the reliability in the present model for partial-porous case modelling.

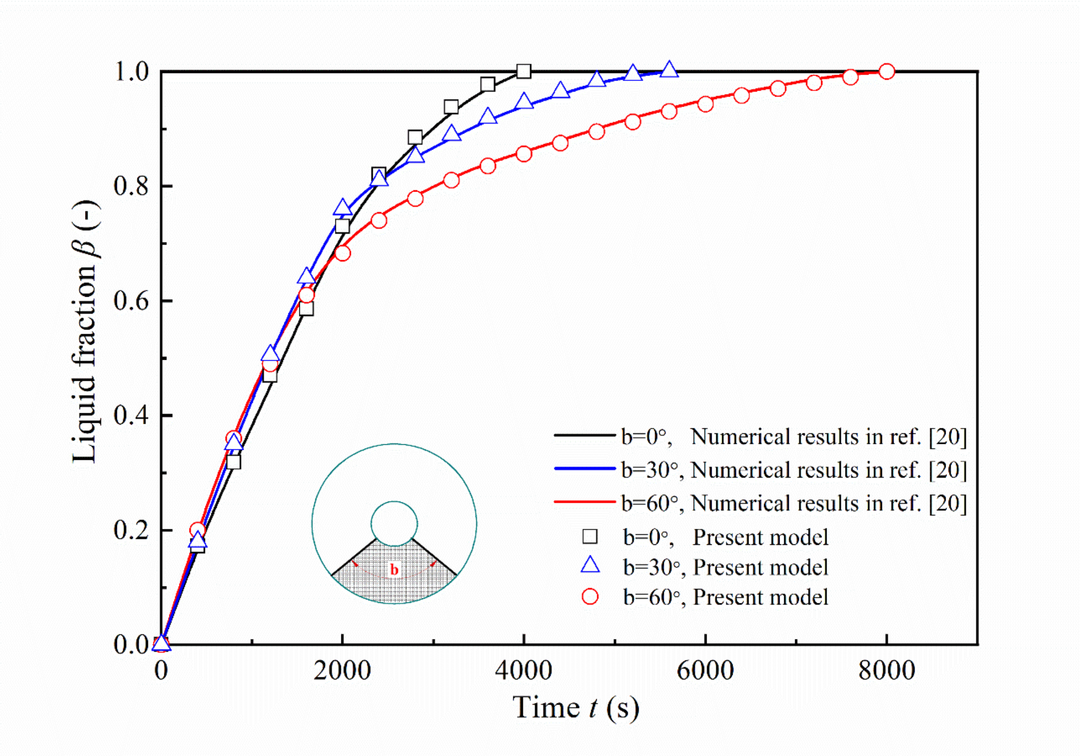

Figure 4. Model reliability for the partial-porous case.

Figure 5 presents the verification and validation of the full-porous model with the experimental results obtained from [41] A copper foam mixed with paraffin wax was used as storage medium and fully filled into a rectangular tank with dimensions of 200 mm in length and 50 mm in height. A constant heat flux is given from the bottom surface and the temperature variation at position of 8 mm above the heating surface is recorded for comparison. It can be seen from Figure 5 that both the present modelling results and experimental data show the PCM starting to melt around 1100 s and completing the charging process around 3900 s. A small deviation between the present model and experimental results has been obtained, thus establishing the reliability in the current model for the full-porous case simulation. The deviation between the present predictions and numerical results in [41] is associated with the paraffin melting temperature difference used in these two models. In [41], the melting point of PCM was taken as a constant value, whereas a melting range of 321-335 K was adopted in the present simulation. This leads to a relatively slant temperature curve over the melting process, and thus a reasonably good consistence of the present model with experimental results.

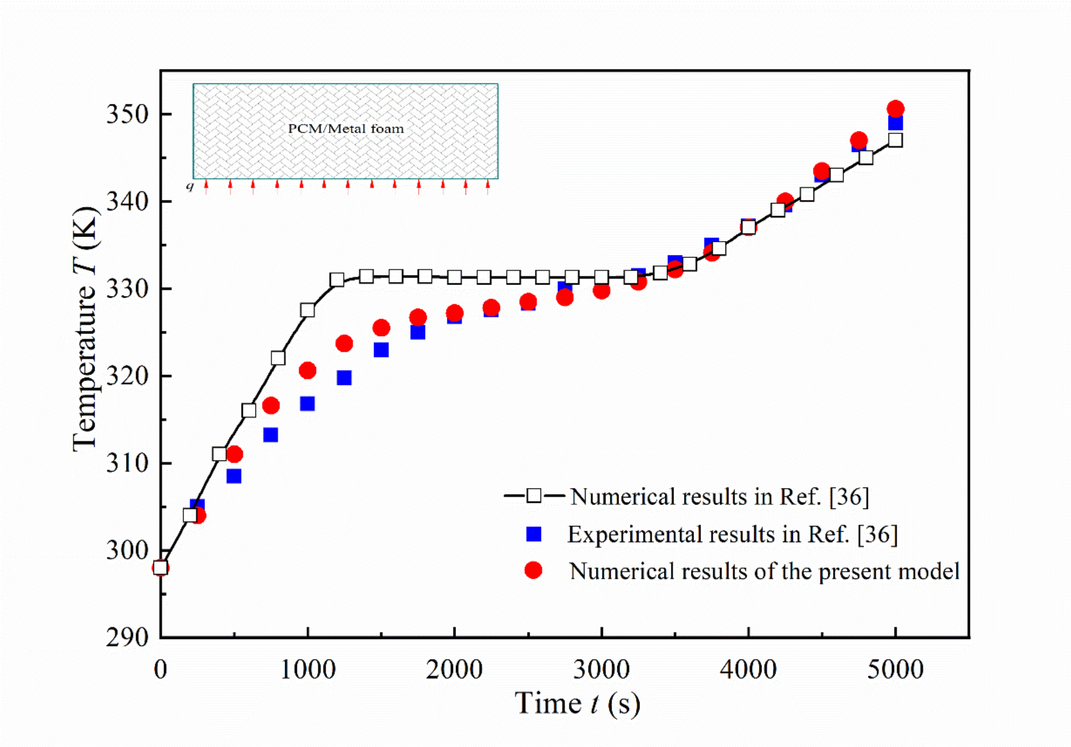

Figure 5. Model reliability for the full-porous case.

3. Results and discussion

3.1 Additive manufactured topology optimised device and experiment validation

In this work, selective laser melting (SLM) metallic additive manufacturing technique was applied to manufacture the topology optimised fins. The additive manufactured device is used to validate numerical simulations and demonstrate the manufacturability of topology optimised fins in reality. As illustrated in Figure 6, by extruding the 2D topology optimised single-tube design along axial direction and connected by pipes at both ends, the design is converted to a 3D device that can be manufactured. An aluminium alloy (Al-5 % Cu) with high thermal conductivity was used as the fin material. Figure 7 (a) demonstrates the final product of additive manufactured topology optimised fins. The features of fin structures can be well reproduced by additive manufacturing, and ready for experimental testing. As illustrated in Figure 7 (b), the additive manufactured device is inserted into an acrylic shell for experimental tests.

The materials and parameters in experiments were kept the same with simulations. For running experiments, the shell was filled up with liquid PCMs (RT25 HC). The PCM was solidified to T_{ini}=294.5 K by connecting to a chiller with a temperature stability of ±0.2 °C. During experiments, the high temperature fluid with a constant temperature (T =308 K) flow through the central pipe, and the PCM is gradually melted. The temperature at different positions within PCM is recorded during the whole process. Detailed descriptions of this experimental system and test procedure have been presented in our previous work [36].

Figure 8 depicts the temperature evolutions at different measurement positions during the whole melting process. The four temperature measurement points in Figure 8 (a) are numbered by 1, 2, 3 and 4 and annotated by different colours in accordance with the curves in Figure 8 (b). In this figure, the CFD simulation results are compared with experimental measurements. The temperature evolutions of numerical simulations and experimental measurements show same tendency. The slight difference between experiments and simulations is likely because of the average physical properties adopted in simulations.

It is worthy to notice that the temperature values at these four measurement points have different trends. As illustrated in Figure 8 (b), the temperature at point 1 and 2 in the lower region rises sharply to the melting range at the beginning. After 500 s, the PCM at these two points are in fully melted states with slowly rising temperature trends afterwards. In the upper region, the temperature evolutions at point 3 and 4 are slower and have three distinguished stages. For point 3, at the initial stage (0-1200 s), the PCM is solid with a constant temperature of around 295 K. After that, the temperature gradually rises to 303 K, and it transforms from solid phase to liquid phase. This is followed by a relatively constant temperature stage as the PCM is totally melted. The temperature at point 7 shows a similar tendency with point 3 but a slower process to be fully melted.

The PCMs of point 1 and 2 in the lower region are near the conductive fins that can be rapidly melted, while point 3 and 4 in a convection dominated region have different heat transfer mechanisms and temperature profiles. The results in Figure 8 testify that the modelling assumptions adopted here can be used to predict the melting process in the system. In the following, CFD simulations were used to further analyse the temperature and liquid fraction evolutions during melting and to compare the performance of different systems.

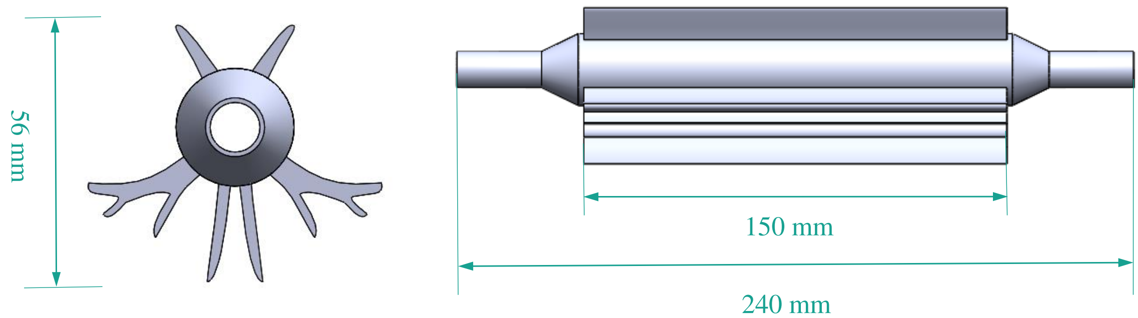

Figure 6. Schematic of the additive manufactured energy storage device with topology optimised fins.

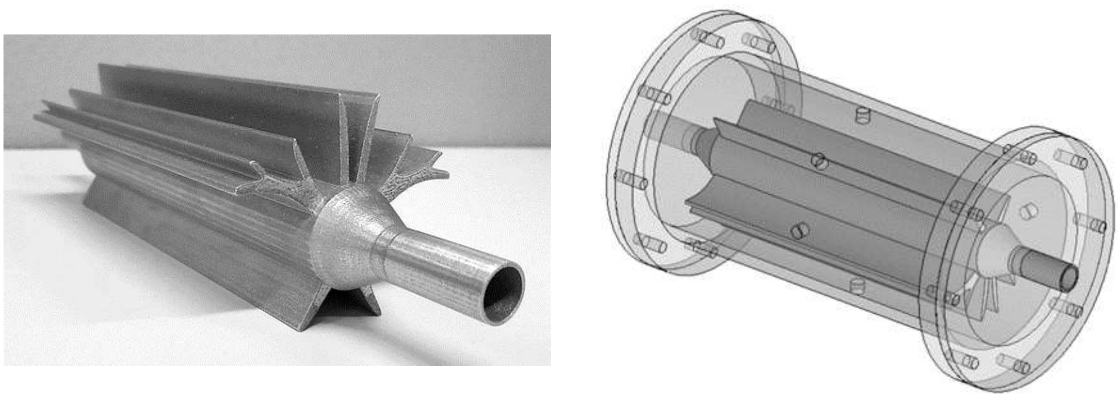

(a) Additive manufactured fins (b) 3D design of the device

Figure 7. Additive manufactured topology optimised fins and 3D design of the energy storage device.

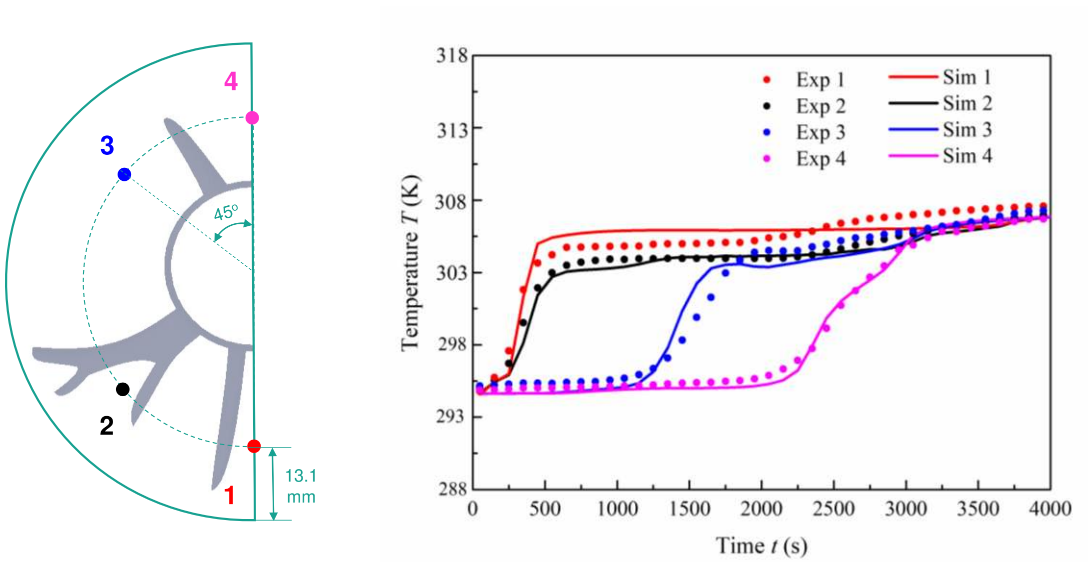

(a) Measurement points (b) Temperature profiles

Figure 8. Comparison of the experimental results and numerical simulations of the measured temperatures.

3.2 Numerical simulation results

3.2.1 Topology optimised fins

Figure 9 presents the temperature and liquid fraction profiles of the topology optimised fins for single-tube configuration. At the beginning stage, the melting region occurs around the fins and it gradually grows. After 3200 s, the solid phase only remains in the bottom and central near wall region. The PCM is completely melted at about 3900s. Figure 10 illustrates the corresponding velocity profiles. It is clear to see that the convection eddies occur in the upper region and the optimised fin configurations are helpful to redirect the flows, while in the region below the pipe the velocity is negligible and the melting is dominated by conduction.

The temperature and liquid fraction profiles of the four-tube topology optimised fins are illustrated in Figure 11. The melt fronts initiate along the fins of the four pipes, and gradually spread to the whole region. After 1600 s, the solid PCM mainly remains in the bottom region and is completely melted at about 2400 s. As shown in Figure 12, high velocities can be observed near the fin regions at the beginning. Due to the strong natural convection, the PCM in the upper region has been melted completely after 1600 s. At this time point, the melting front reaches the bottom regions, and liquid PCM start to move upwards as illustrated in Figure 12. In the following section, the liquid fraction variations are obtained and compared with the metal foam system.

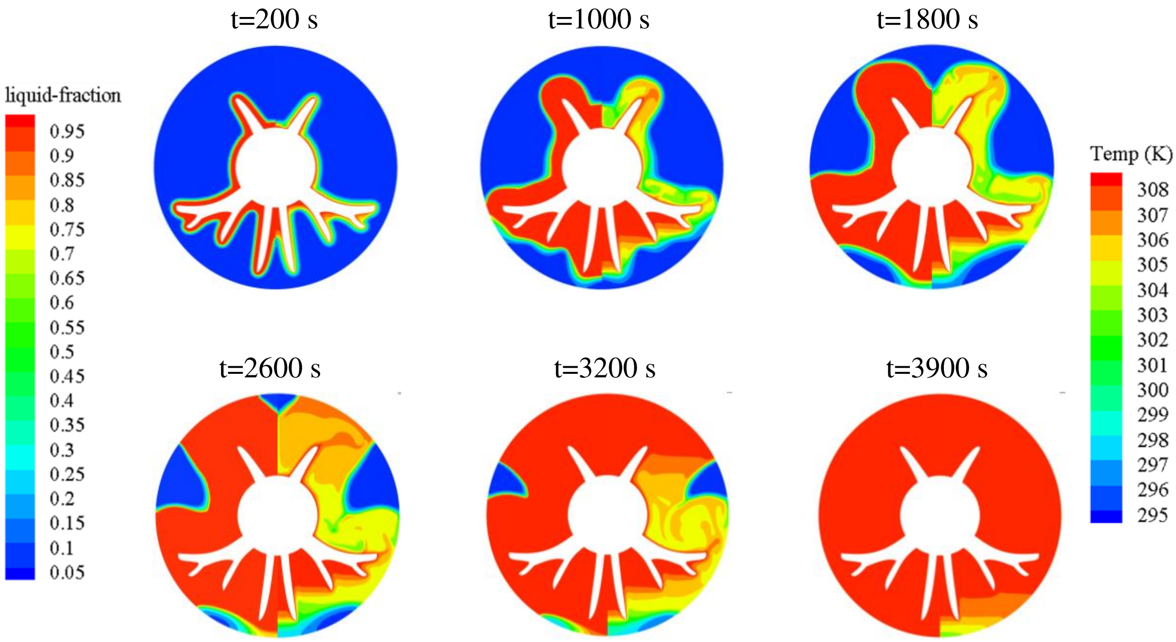

Figure 9. Liquid fraction (left side) and temperature (right side) profiles of the topology optimised fins for single-tube device.

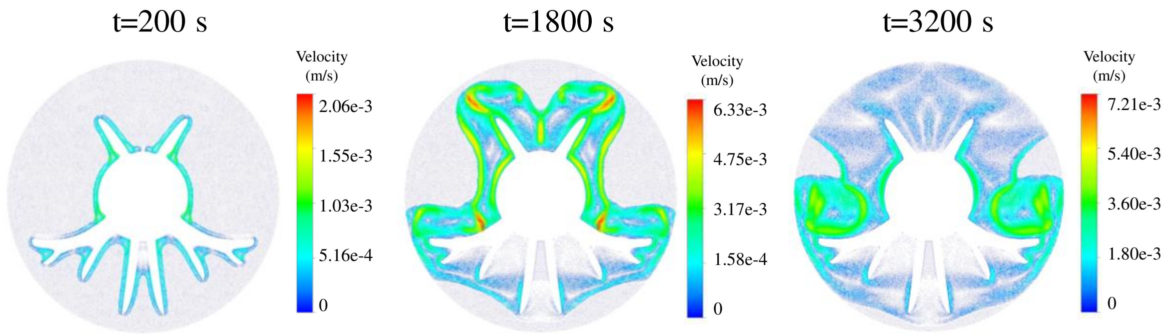

Figure 10. Velocity profiles of the topology optimised fins for single-tube device.

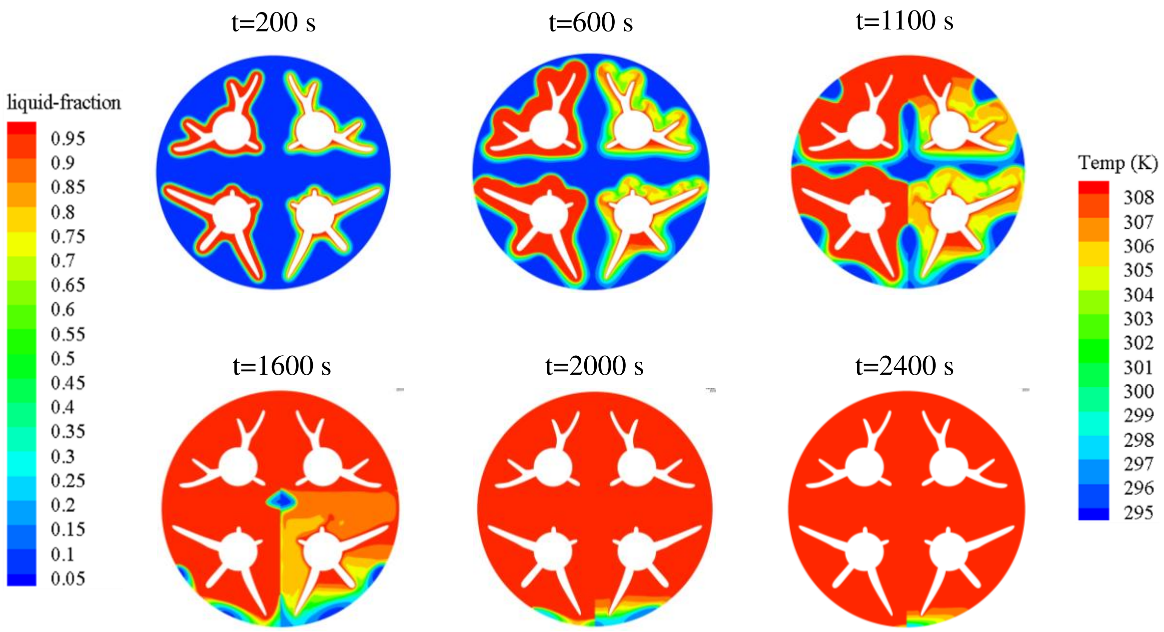

Figure 11. Liquid fraction (left side) and temperature (right side) profiles of the topology optimised fins for four-tube device.

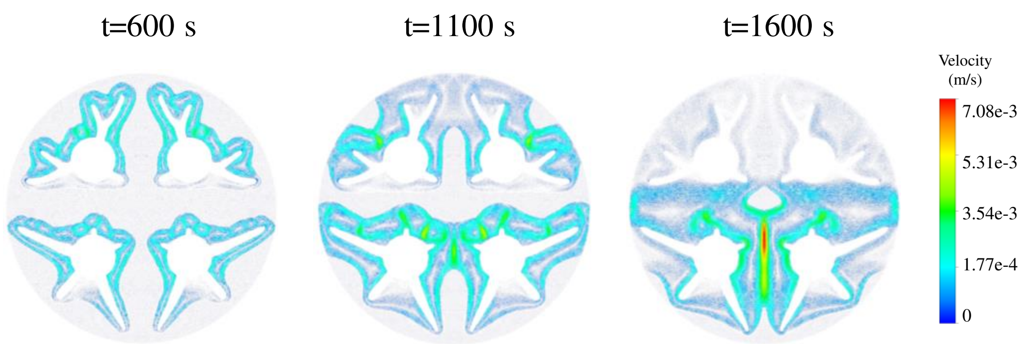

Figure 12. Velocity profiles of the topology optimised fins for four-tube device.

3.2.2 Conductive foams

Figure 13 shows the contours of temperature and liquid fraction for single-tube device containing half-foam structure. One can see that the natural convection and thermal conduction respectively dominates the heat transfer process in the upper and lower parts of the device. At the initial melting stage (*t*=100 s), the melting process within the device is mainly governed by thermal conduction and only a small amount of PCM close to the heating tube melts. As the melting process evolves, more solid material melts, leading to the increase of liquid phase in the device. Owing to the existed density between the solid and liquid phases, natural convection starts to play an important role in driving the material melting, which in turn leads to the acceleration of material melting in the upper part. Over the melting duration of 500-2000 s, intense natural motion is apparent, achieving fast melting rate in the non-foam zone. From Figure 13, it can also be seen that, due to the implementation of metal foam, the effective thermal conductivity in the lower part is higher than that in the upper part, which leads to a faster melting rate in the foam filled field.

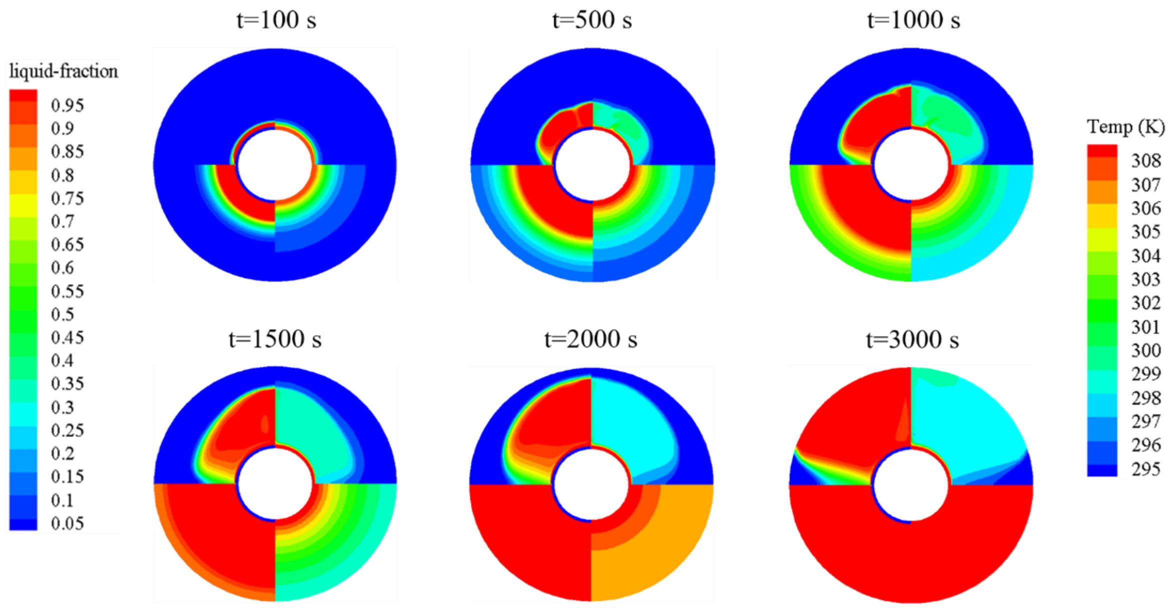

Figure 13. Contours of liquid fraction (left side) and temperature (right side) for single-tube device containing half-foam structure.

Figure 14 displays the contours of temperature and liquid fraction for four-tube device containing half-foam structure. It can be seen that, similar to single-tube device, the melting process in the lower part of the four-tube device is mainly governed by thermal conduction while that occurred at the upper part is first dominated by thermal conduction and later by natural convection. Because of the high effective thermal conductivity, the average temperature in the lower part increases faster than that in the lower part. Giving the contrastive analysis of the contours shown in Figures 13 and

14, one can see a relatively faster melting process and a low extent of thermal stratification in the four-tube device than that in single-tube device. At the same melting moment, i.e., t=500 s and t=2000 s, the average temperature and liquid fraction in the four-tube configuration are apparently higher than that in the single-tube configuration, which implies a higher heat transfer rate in the four-tube device in comparison with the single-tube device. This observation indicates, for a given heat transfer surface and same volume of metal foam implemented in the lower zone, the four-tube configuration achieves a faster melting rate and hence a shorter duration for completing the charging process.

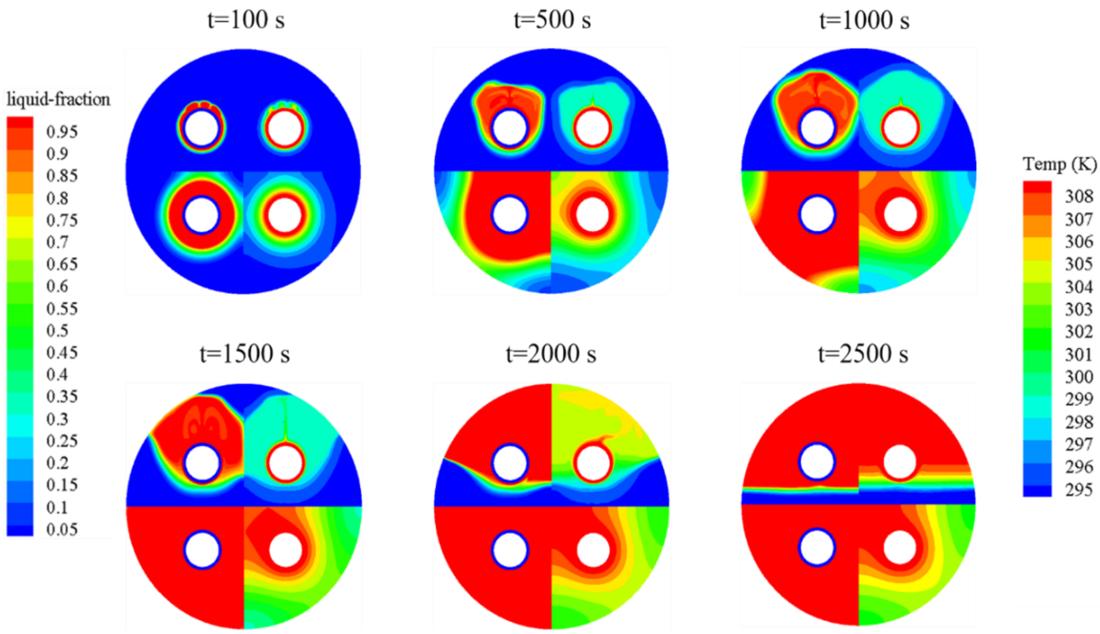

Figure 14. Contours of liquid fraction (left side) and temperature (right side) for four-tube device containing half-foam structure.

For the device containing whole-foam structure, the modelling results are presented in Figure 15. One can see that the natural motion influence is not as evident as that in pure PCM because of the existence of metal foam. For both the single and four-tube devices, the melting process is conduction dominant and there is no large temperature swing existed across the melting front, leading to a broader and uniform mushy zone inside the device. From Figure 15, it can also be observed that, due to the difference in heat transfer tube arrangement, the melting rate between the single and four-tube device is also different. For a fixed heat transfer surface area, an even array of heat transfer tube in the four-tube configuration achieves a more homogeneous heat transfer and hence a higher melting rate than that in the single-tube configuration. To sum up the Figures 13-15, it can be concluded that the insert of the metal foam can be confirmed to enhance the heat transfer performance of the PCM based device, and the performance enhancement caused by implementation of metal foam is far larger than that could be achieved through natural convection.

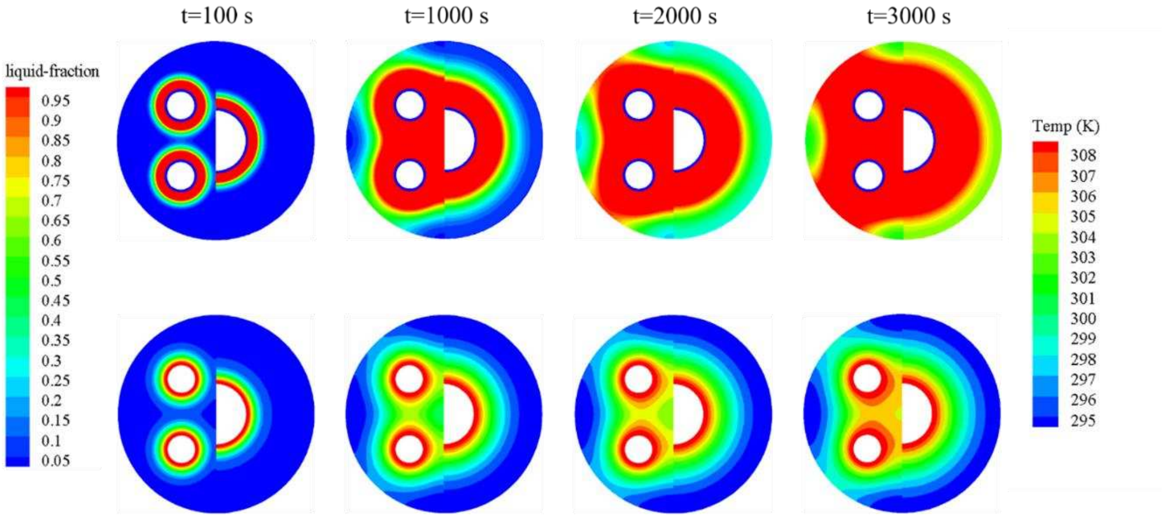

Figure 15. Contours of and liquid fraction (up) and temperature (bottom) for the device containing whole foam structure. The four-tube device results are shown on the left side, and the single-tube device on the right side.

3.3 Comparison analysis

In this section, for making a better quantitative analysis, the charging time of conventional devices without any enhancement structures is also calculated by numerical simulations. The conventional device has the same shell-and-tube configuration as shown in Figure 1. This device is numerically analysed to benchmark the performance of different thermal enhancement techniques in this work. As the conventional device has relative long melting time, the results are not directly illustrated in the following figures. Figure 16 shows the variation of liquid fraction with time for the single-tube device containing different enhancement structures. One can see that, compared with the device containing no additional structure, the melting rate inside the device can be significantly increased with the use of enhanced structures. For the device containing topology structure, the whole charging process is finished around 3800 s, which achieves the reduction of total charging time by more than 88% in comparison with the conventional device without enhanced structures whose charging time is 33000 s. For the half-foam structured device, a rapid melting rate is also observed in which the melting process is completed around 4250 s, denoting 86% of melting time could be saved. The melting process in the whole-foam structured device lasts 4850 s, suggesting only 84% melting time reduced compared to the device with no enhanced structure.

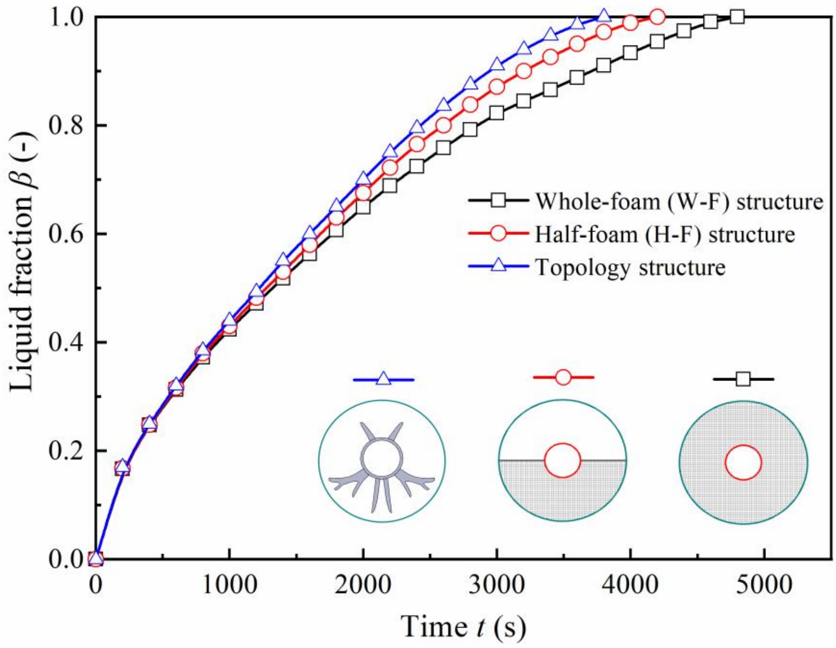

Figure 16. Time evolutions of the liquid fraction for the single-tube configuration containing different structures.

Figure 17 presents the time evolution of the liquid fraction in the four-tube device with the use of different enhancement structures. One can see a similar trend in the liquid fraction as a function of time at different structured devices to these shown in Figure 16 as describe above. The melting rate in the topology structured device is the highest while that in the whole-foam structured device is the lowest. Compared with the conventional device, the whole melting process for the device containing topology, half-foam and whole-foam structures is respectively reduced 88.5%, 86.8% and 83.4%. An inspection of Figure 17 also finds that, although the whole melting process in whole-foam structured device is the longest, it has the highest melting rate at initial melting stage over 0-1200 s among all the three structured devices. The main reason lies in the heat transfer domination mechanism difference among the three devices. Unlike other two structured devices where natural convection plays an important role in melting process, the heat transfer in the whole-foam structured device is completely dominated by the thermal conduction. In the initial stage, a large temperature difference is apparent and hence a high heat transfer rate is observed in the W-H structured device. With the evolve of the melting process, the temperature difference is gradually diminished, leading to a low heat transfer rate in the device and hence a slow melting process at the late charging stage.

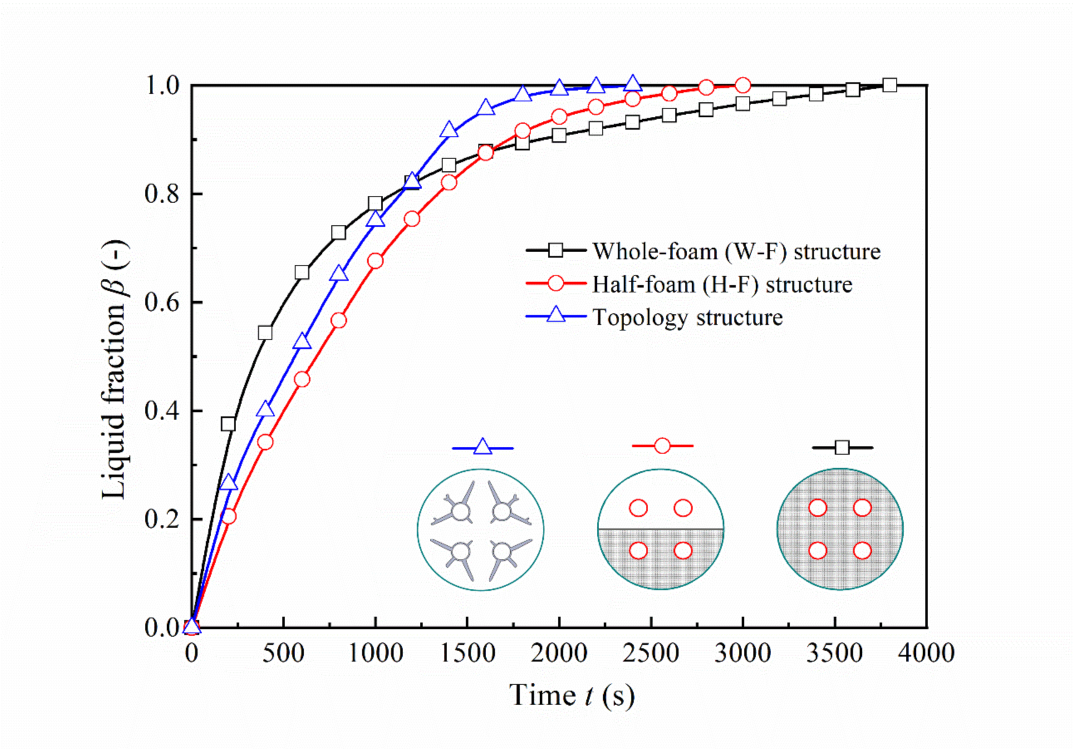

Figure 17. Time evolutions of the liquid fraction for the four-tube configuration containing different structures.

The preliminary observations of the Figures 16 and 17 indicate that the acceleration of melting process with the use of topology structure is the highest while that with the use of whole-foam structure is the lowest, denoting the highest heat transfer rate in the topology structured device and the lowest heat transfer rate in the whole-foam structured device. The use of topology structure seems to be the optimal enhancement approach for both the sing-tube and four-tube devices. However, using the reduction extent of melting time as the output performance is not enough to disclose the superiority of the enhancement configuration. As reported in Xu's work [23, 25] , the indicator of charging time can only give partial appraisement for the enhancement approach and is insufficient to give a full evaluation. Other criteria are therefore required to achieve comprehensive assessment for a PCM based device with different performance enhancement methods.

Figure 18 presents the dimensionless average TES rate and TES density of different enhancement structures. One can see that due to the constant volume of the enhancement additive, the q'_{ave} in single-tube configuration is equal to the four-tube configuration, which is decreased to 0.46 times in comparison with the non-enhancement configuration. For p'_{ave}, the value in the single-tube and four-tube configurations containing topology, whole-foam and half-foam structures can be respectively increased to 4.3, 3.3 and 3.9 times, and 5.8, 3.6 and 4.7 times compared to the configuration with no enhancement. This indicates that all these three enhancement approaches in both configurations can effectively accelerate the TES rate with the highest p'_{ave} appearing in the topology structure and the lowest p'_{ave} in the whole-porous structure. For a fixed amount of additive, the p'_{ave} in four-tube configuration is higher than that in single-tube configuration, denoting a better charging performance in four-tube configuration. An inspect of the results in Figure 18 can also find that the use of topology structure achieves the largest difference in p'_{ave} between the single-tube and four-tube configurations while the full-porous structure gives the lowest difference in p'_{ave}. The reason for the variation in the full-porous structured device is easily understood; the heat transfer in porous region is dominated by thermal conduction and hence a nearly equal heat transfer rate is achieved in both the single-tube and four-tube devices containing the same volume metal foam. The occurrence of the difference in topology structured configuration can be attributed to the topological optimization and heat transfer tube arrangements in the device. A more uniform heat transfer in the four-tube configuration is appeared due to the more even distribution of the topology structure and heat transfer tube, and hence a faster heat transfer rate can be obtained in four-tube configuration compared to the single-tube configuration.

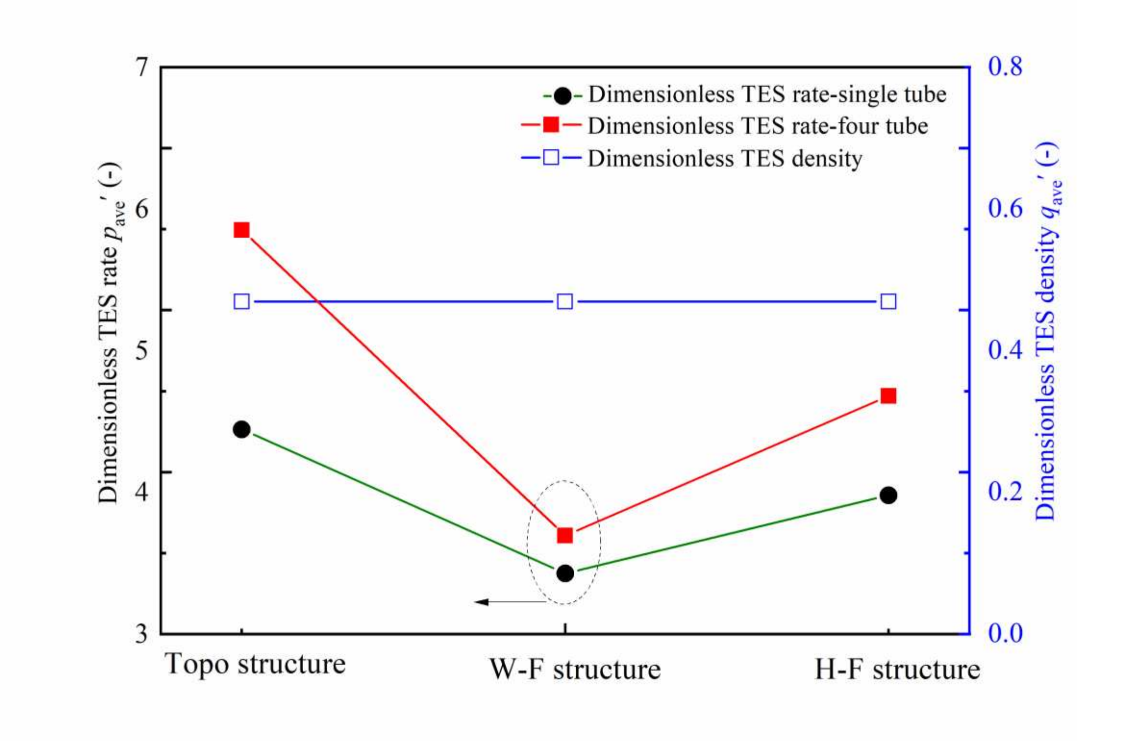

Figure 18. Dimensionless average TES rate and TES density of different structured configurations.

In Xu's work [25] , a more comprehensive parameter of TES rate per material cost, relating to the ratio between the TES rate and material unit price was proposed to compare the enhancement efficiency of the PCM based device from the perspective of material cost. In general, ideal enhancement structure should not only possess the ability to endow the device with high heat transfer performance but also has the low cost. In real applications, however, the preeminent additions are either constitutionally expensive or hard to produce with high manufacture cost. Therefore, the right balance should be struck between the performance and the cost for a PCM based device containing enhanced structures. In this work, such a parameter of p_{c} and its dimensionless form p_c' is defined by Equations (32) and (33) for determining the device input-output performance. Figures 19 and 20 show the variations of p_c' with R for different structures in the single-tube and four-tube configurations, respectively. One can see that the unit price ratio R plays an important role in selecting the optimal structure. When R is equal to 1, the economic efficiency of p_c in the enhanced configuration can be enhanced to 3-5 times in comparison with the configuration containing no enhancement structure. With the increase of R, the economic efficiency of all the enhanced structures in both the single-tube and four-tube configurations is decreased with different extents. When R is in the range of 1-6, the economic efficiency in the topology structure is the highest while that in the whole-foam structure is the lowest, indicating the topology structure is the best option and the whole-foam structure is always not the best solution. This is agreement with the results discussed in Figures 16-18 that the topology structure achieves the best heat transfer performance in the device. With the further increasing R, p_c' in both the single-tube and four-tube configurations will be less than 1 when R is larger than 6. This indicates that, for a given enhanced structure with price more than 6 times higher than the PCM, the economic efficiency of the device with enhancement addition will be lower than that in the device with no enhancement. In such cases, a desired utilization efficiency of the material cost will not be realized. This observation, together with the results presented in Figures 16-18, suggest that the parameter of the TES rate per unit price could be quantitatively used for evaluating the device input-output efficiency and pointing the optimal enhancement design from the economic perspective. The amount of enhancement addition and its geometry as well as arrangement should be meticulously optimized with the synthetical consideration of the heat transfer rate and material cost. Although the manufacturing technology and the associated cost for using porous metal foam is mature and rational at the present stage, it does not have the optimal heat transfer enhancement efficiency. As the current metal additive manufacturing is mainly used for customised parts, the costs are still not within a reasonable range. For the implementation of additive manufacturing technology, the insert of topopology structure would be an economical solution to realize the combined enhancement of heat transfer performance and material utilization efficiency if the unit price ratio R between the structure and the PCM can be controlled to less than 6.

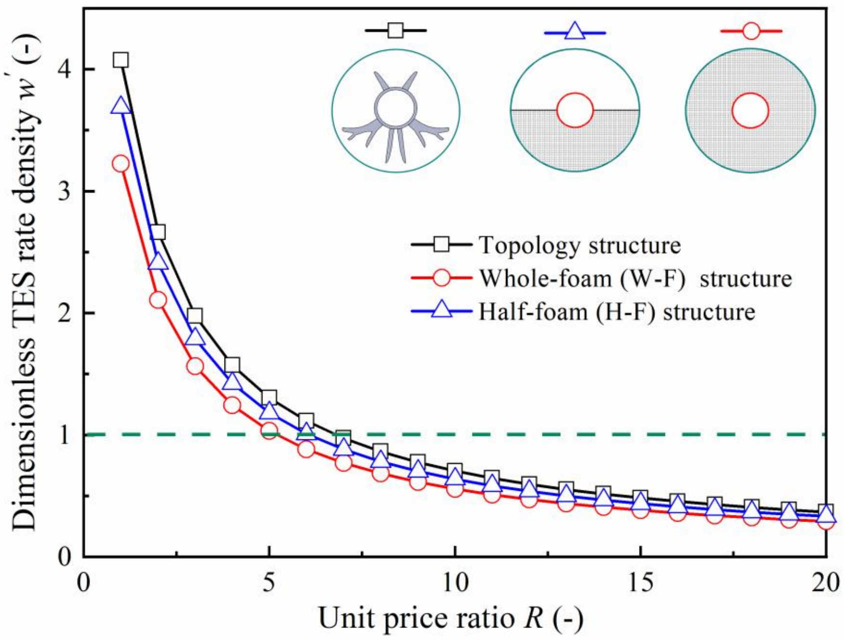

Figure 19. Variation of dimensionless average TES rate per material cost p_c' with unit price ratio R for different structures in singe-tube configuration.

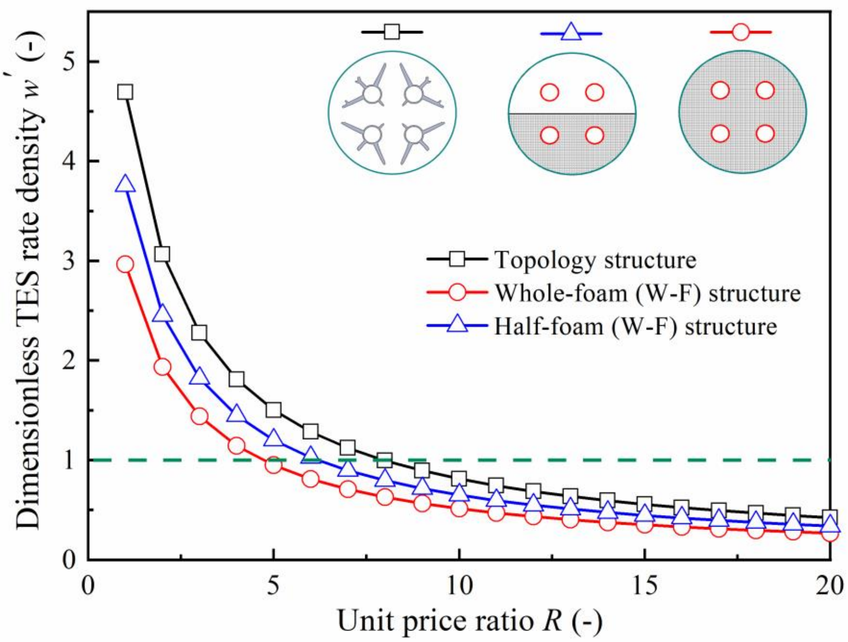

Figure 20. Variation of dimensionless average TES rate per material cost p_c' with unit price ratio R for different structures in four-tube configuration.

4. Conclusions (Add more quantitative results)

In this work, different melting enhancement techniques i.e. topology optimised structures and conductive foam structures for the LHTES system are investigated by CFD simulations.

The SLM metallic additive manufactured device are used to demonstrate the manufacturability of topology optimised structures and to validate the numerical simulations. The temperature and liquid fraction evolutions during melting are analysed considering different topology optimised fin configurations. The corresponding conductive foam structures including whole-foam structure and half-foam structure are further analysed. For the first time, these different structures are quantitatively compared from perspectives of device performance and economy. The comparison results show that the topology optimised structure can achieve the highest TES storage rate. The highest dimensionless TES rate p'_{ave} is 5.8 for the four-tube topology optimised structure, while the lowest p'_{ave} is 3.3 for the whole-foam half single-tube configuration. However, from a perspective of material and device cost, the unit price ratio between the enhance technique and PCM material has to be controlled to less than 6 (R<6) to become an economical solution. The results presented here provide an insight to comprehensively evaluate different melting enhancement techniques.

As a perspective it would be useful to further advance the structure design, performance and economy evaluation to typical applications in future.

Nomenclature

Abbreviations

2D	Two-dimensional
3D	Three-dimensional
CFD	Computational fluid dynamics
FVM	Finite volume method
HTF	Heat transfer fluid
LHTES	Latent heat thermal energy storage
PCM	Phase change material
SLM	Selective laser melting
TES	Thermal energy storage

Symbols

A_m	Mushy constant, $kg \cdot m^{-3} \cdot s^{-1}$
A_{sf}	Surface area density, m^{-1}

a Permeability, m^2

a Unit price

C_i Inertia coefficient, $W \cdot m^{-2} \cdot K^{-1}$

C_p Specific heat, $kJ \cdot kg^{-1} \cdot K^{-1}$

d_f Cell ligament diameter, m

d_p Pore diameter, m

g Gravity, $m \cdot s^{-2}$

h Heat transfer coefficient

k Thermal conductivity, $W \cdot m^{-1} \cdot K^{-1}$

L Latent heat, $kJ \cdot kg^{-1}$

m Mass, kg

Pr Prandtl number

p Pressure, Pa

p_{ave} Average TES rate, $J \cdot s^{-1}$

p_c Average TES rate per material cost, $J \cdot s^{-1} \cdot \$^{-1}$

p_{ave}' Dimensionless average TES rate

p_c' Dimensionless average TES rate per material cost

Q TES capacity, J

q_{ave} Average TES density, $J \cdot kg^{-1}$

q_{ave}' Dimensionless average TES density

Ra Rayleigh number

R Unit price ratio

S Material cost

T Temperature, K

t Time, s

t_m Melting time, s

u, v Velocity, $m \cdot s^{-1}$

w TES rate density, $J \cdot kg^{-1} \cdot s^{-1}$

w' Dimensionless TES rate density

x, y Coordinates

608 *Greek letters*

α Thermal diffusivity, $m^2 \cdot s^{-1}$

β Liquid fraction

γ Thermal expansion coefficient, K^{-1}

ε Foam porosity

μ Dynamic viscosity, $kg \cdot m^{-1} \cdot s^{-1}$

v Kinematic viscosity, $m^2 \cdot s^{-1}$

ρ Density, $kg \cdot m^{-3}$

ω Constant number

Subscript

0 Basic case without enhancement

f Fluid

fe Effective thermal conductivity of fluid

l Liquid phase

M Metal enhancement material

P Phase change material

ref Reference value

s Solid phase

sf Between solid and fluid

se Effective thermal conductivity of solid

td Thermal dispersion

Acknowledgement

The authors would like to acknowledge the financial support from the high-end talents development program of Beijing University of Technology. They would also like to acknowledge Dr. Adriano Sciacovelli and Prof. Yongliang Li from Birmingham Centre for Energy Storage (BCES), University of Birmingham for their useful support and discussion.

References

[1] Q. Li, C. Li, Z. Du, F. Jiang, Y. Ding, A review of performance investigation and enhancement of shell and tube thermal energy storage device containing molten salt based phase change materials for medium and high temperature applications, Applied Energy 255 (2019) 113806.

[2] J.C. Choi, S.D. Kim, Heat-transfer characteristics of a latent heat storage system using $MgCl_2 \cdot 6H_2O$, Energy 17(12) (1992) 1153-1164.

[3] S. Tiari, S. Qiu, Three-dimensional simulation of high temperature latent heat thermal energy storage system assisted by finned heat pipes, Energy Conversion and Management 105 (2015) 260-271.

[4] A. Rozenfeld, Y. Kozak, T. Rozenfeld, G. Ziskind, Experimental demonstration, modeling and analysis of a novel latent-heat thermal energy storage unit with a helical fin, International Journal of Heat and Mass Transfer 110 (2017) 692-709.

[5] A. Sciacovelli, F. Gagliardi, V. Verda, Maximization of performance of a PCM latent heat storage system with innovative fins, Applied Energy 137 (2015) 707-715.
[6] M. Hosseini, A. Ranjbar, M. Rahimi, R. Bahrampoury, Experimental and numerical evaluation of longitudinally finned latent heat thermal storage systems, Energy and Buildings 99 (2015) 263-272.
[7] W.-W. Wang, L.-B. Wang, Y.-L. He, Parameter effect of a phase change thermal energy storage unit with one shell and one finned tube on its energy efficiency ratio and heat storage rate, Applied Thermal Engineering 93 (2016) 50-60.
[8] J.N. Chiu, V. Martin, Submerged finned heat exchanger latent heat storage design and its experimental verification, Applied Energy 93 (2012) 507-516.
[9] Z. Khan, Z.A. Khan, An experimental investigation of discharge/solidification cycle of paraffin in novel shell and tube with longitudinal fins based latent heat storage system, Energy conversion and management 154 (2017) 157-167.
[10] M. Kazemi, M. Hosseini, A. Ranjbar, R. Bahrampoury, Improvement of longitudinal fins configuration in latent heat storage systems, Renewable Energy 116 (2018) 447-457.
[11] H.B. Mahood, M.S. Mahdi, A.A. Monjezi, A.A. Khadom, A.N. Campbell, Numerical investigation on the effect of fin design on the melting of phase change material in a horizontal shell and tube thermal energy storage, Journal of Energy Storage 29 (2020) 101331.
[12] A. Pizzolato, A. Sharma, K. Maute, A. Sciacovelli, V. Verda, Topology optimization for heat transfer enhancement in latent heat thermal energy storage, International Journal of Heat and Mass Transfer 113 (2017) 875-888.
[13] A. Pizzolato, A. Sharma, K. Maute, A. Sciacovelli, V. Verda, Design of effective fins for fast PCM melting and solidification in shell-and-tube latent heat thermal energy storage through topology optimization, Applied energy 208 (2017) 210-227.
[14] A. Pizzolato, A. Sharma, R. Ge, K. Maute, V. Verda, A. Sciacovelli, Maximization of performance in multi-tube latent heat storage–Optimization of fins topology, effect of materials selection and flow arrangements, Energy 203 (2020) 114797.
[15] Z. Liu, Y. Yao, H. Wu, Numerical modeling for solid–liquid phase change phenomena in porous media: Shell-and-tube type latent heat thermal energy storage, Applied energy 112 (2013) 1222-1232.
[16] M. Esapour, A. Hamzehnezhad, A.A.R. Darzi, M. Jourabian, Melting and solidification of PCM embedded in porous metal foam in horizontal multi-tube heat storage system, Energy conversion and management 171 (2018) 398-410.
[17] Z. Wu, C. Zhao, Experimental investigations of porous materials in high temperature thermal energy storage systems, Solar Energy 85(7) (2011) 1371-1380.
[18] J. Yang, X. Du, L. Yang, Y. Yang, Numerical analysis on the thermal behavior of high temperature latent heat thermal energy storage system, Solar energy 98 (2013) 543-552.
[19] M. Iasiello, M. Mameli, S. Filippeschi, N. Bianco, Simulations of paraffine melting inside metal foams at different gravity levels with preliminary experimental validation, Journal of Physics: Conference Series, IOP Publishing, 2020, p. 012008.
[20] J. Yang, L. Yang, C. Xu, X. Du, Numerical analysis on thermal behavior of solid–liquid phase change within copper foam with varying porosity, International Journal of Heat and Mass Transfer 84 (2015) 1008-1018.
[21] L. Pu, S. Zhang, L. Xu, Z. Ma, X. Wang, Numerical study on the performance of shell-and-tube thermal energy storage using multiple PCMs and gradient copper foam, Renewable Energy 174 (2021) 573-589.
[22] C. Yang, Y. Xu, X. Cai, Z.-J. Zheng, Effect of the circumferential and radial graded metal foam on horizontal shell-and-tube latent heat thermal energy storage unit, Solar Energy 226 (2021) 225-235.
[23] Y. Xu, Q. Ren, Z.-J. Zheng, Y.-L. He, Evaluation and optimization of melting performance for a latent heat thermal energy storage unit partially filled with porous media, Applied energy 193 (2017) 84-95.

[24] V. Joshi, M.K. Rathod, Thermal performance augmentation of metal foam infused phase change material using a partial filling strategy: An evaluation for fill height ratio and porosity, Applied Energy 253 (2019) 113621.
[25] Y. Xu, M.-J. Li, Z.-J. Zheng, X.-D. Xue, Melting performance enhancement of phase change material by a limited amount of metal foam: Configurational optimization and economic assessment, Applied energy 212 (2018) 868-880.
[26] X. Yang, J. Yu, T. Xiao, Z. Hu, Y.-L. He, Design and operating evaluation of a finned shell-and-tube thermal energy storage unit filled with metal foam, Applied Energy 261 (2020) 114385.
[27] J. Guo, Z. Liu, Z. Du, J. Yu, X. Yang, J. Yan, Effect of fin-metal foam structure on thermal energy storage: An experimental study, Renewable energy 172 (2021) 57-70.
[28] J. Khodadadi, S. Hosseinizadeh, Nanoparticle-enhanced phase change materials (NEPCM) with great potential for improved thermal energy storage, International communications in heat and mass transfer 34(5) (2007) 534-543.
[29] A. Mohamad, Myth about nano-fluid heat transfer enhancement, International Journal of Heat and Mass Transfer 86 (2015) 397-403.
[30] A.A.R. Darzi, M. Jourabian, M. Farhadi, Melting and solidification of PCM enhanced by radial conductive fins and nanoparticles in cylindrical annulus, Energy conversion and management 118 (2016) 253-263.
[31] J.M. Mahdi, E.C. Nsofor, Melting enhancement in triplex-tube latent thermal energy storage system using nanoparticles-fins combination, International Journal of Heat and Mass Transfer 109 (2017) 417-427.
[32] A. Pizzolato, A. Sharma, R. Ge, K. Maute, V. Verda, A. Sciacovelli, Maximization of performance in multi-tube latent heat storage–Optimization of fins topology, effect of materials selection and flow arrangements, Energy (2019).
[33] V.R. Voller, M. Cross, N. Markatos, An enthalpy method for convection/diffusion phase change, International journal for numerical methods in engineering 24(1) (1987) 271-284.
[34] Rubitherm Technologies GmbH RT25HC data sheet
https://www.rubitherm.eu/media/products/datasheets/Techdata_-RT25HC_EN_05092018.PDF.
[35] S. Khanna, K. Reddy, T.K. Mallick, Optimization of solar photovoltaic system integrated with phase change material, Solar Energy 163 (2018) 591-599.
[36] R. Ge, G. Humbert, R. Martinez, M.M. Attallah, A. Sciacovelli, Additive manufacturing of a topology-optimised multi-tube energy storage device: Experimental tests and numerical analysis, Applied Thermal Engineering (2020) 115878.
[37] V.V. Calmidi, R.L. Mahajan, Forced convection in high porosity metal foams, J. Heat Transfer 122(3) (2000) 557-565.
[38] R.L. Mahajan, Transport phenomena in high porosity metal foams, Ph. D. thesis, University of Colorado, 2001.
[39] J.G. Georgiadis, I. Catton, Dispersion in cellular thermal convection in porous layers, International journal of heat and mass transfer 31(5) (1988) 1081-1091.
[40] S.W. Churchill, H.H. Chu, Correlating equations for laminar and turbulent free convection from a horizontal cylinder, International journal of heat and mass transfer 18(9) (1975) 1049-1053.
[41] Y. Tian, C.-Y. Zhao, A numerical investigation of heat transfer in phase change materials (PCMs) embedded in porous metals, Energy 36(9) (2011) 5539-5546.